PAPER

Check for updates

NiO- and MnO-nanoparticle-modified pyrogallol-formaldehyde-derived carbon matrix

N. Ben Mansour, [ID] *[a] Rageh K. Hussein,[b] M. Hjiri[b] and L. El Mir[a]

A pyrogallol-formaldehyde-derived carbon matrix (CM) and its nanocomposites modified with nickel oxide (NiO) and manganese oxide (MnO) nanoparticles were synthesized *via* a sol–gel method. X-ray diffraction revealed the amorphous nature of the carbon matrix, the presence of metallic Ni and the preserved structural stability of MnO. SEM images revealed a highly porous morphology favorable for nanoparticle incorporation, with homogeneous Ni dispersion and MnO nanoparticles showing some clustering. EDX and XPS analyses verified the successful integration of metal oxides and the presence of residual chlorine exclusively in the CM/MnO nanocomposite. Raman spectroscopy showed a progressive increase in structural disorder from CM ($I_D/I_G = 0.76$) to the CM/MnO nanocomposite ($I_D/I_G = 1.53$), consistent with an enhanced defect density and charge carrier sites. Electrical measurements demonstrated semiconducting behavior with improved conductance upon the incorporation of metal oxides. The CM/MnO nanocomposite exhibited the highest conductance and the lowest activation energy (80 meV), attributed to the Mn^{2+}/Mn^{3+} redox activity and chlorine-induced defect formation. Impedance and dielectric studies revealed Maxwell–Wagner-type interfacial polarization with non-Debye relaxation behavior, governed by distinct conduction mechanisms: correlated barrier hopping (CBH) in the CM/NiO nanocomposite and small polaron hopping (SPH) in the CM/MnO nanocomposite. These results highlight the important role of transition metal oxides in electrical conduction and provide valuable insights for designing efficient carbon-based nanocomposites for advanced electronic applications.

1. Introduction

Carbon-based materials are drawing growing interest due to their outstanding properties, such as high electron and thermal transport, excellent chemical stability, tunable porosity and low-cost fabrication.[1–6] These features make them highly promising for diverse technological fields such as electronics, gas capture and sensing devices.[7–11] However, amorphous carbon materials or carbons with limited surface area often suffer from restricted charge carrier mobility and a lack of active sites, which can limit their electronic and dielectric performance.[12,13] To overcome these limitations, embedding transition metal oxide nanoparticles within the carbon framework has proven to be a particularly effective strategy. Transition metal oxides, including nickel oxide (NiO) and manganese oxide (MnO), are of particular interest because of their variable oxidation states, high electronic polarizability and strong electrocatalytic activity.[14–17] When dispersed within a carbon matrix, these oxides can markedly enhance the charge carrier density, interfacial polarization and consequently the overall electrical

conductivity. NiO, a p-type semiconductor, contributes to structural stabilization and controlled electrical transport.[18,19] In contrast, MnO, owing to its Mn^{2+}/Mn^{3+} redox activity, facilitates charge transport through polaron hopping and the generation of active defect sites.[20,21] Moreover, the interplay between metal oxides and the carbon matrix further improves the conductive performance of the resulting nanocomposites, particularly when the oxide nanoparticles are homogeneously dispersed. Among carbon precursors, the pyrogallol-formaldehyde resin provides an efficient synthetic route based on the sol–gel process, enabling the formation of highly porous carbon matrices with uniform texture and controlled morphology.[22–24] The sol–gel technique offers an accessible, economical and efficient route for achieving uniform nanoparticle dispersion and strong inorganic–organic interactions, which are essential for obtaining reproducible and tunable electrical properties.[25–27]

Recently, hybrid nanocomposites derived from carbon and metal oxides have attracted considerable interest because of their synergistic characteristics that combine the high electrical conductivity of carbon materials with the electrochemical activity of transition metal oxides. Among these systems, carbon/NiO and carbon/MnO nanocomposites have been widely investigated for their potential applications in energy storage, catalytic activity and sensing devices. For example, Sivakumar

[a]Laboratory of Physics of Materials and Nanomaterials Applied at Environment, Faculty of Sciences in Gabes, Gabes University, Gabes 6072, Tunisia. E-mail: Benmansour.nabil@yahoo.fr

[b]Physics Department, College of Sciences, Imam Mohammad Ibn Saud Islamic University, Riyadh 11623, Saudi Arabia

et al. described the synthesis of carbon-NiO nanocomposites for the amperometric detection of hydrazine and hydrogen peroxide, demonstrating excellent electrocatalytic activity and sensitivity.[28] Similarly, Justin *et al.* designed a highly porous carbon sphere@nickel oxide core–shell nanocomposite that exhibited remarkable capacitive behavior.[29] Meanwhile, Seitkazinova *et al.* synthesized a porous carbon/NiO composite for high-performance energy storage applications.[30] Furthermore, Singh *et al.* developed nickel oxide nanoparticles/biomass-derived activated carbon composites that served as efficient electrodes for aqueous asymmetric supercapacitors.[31] On the other hand, carbon/MnO nanocomposites have also shown promising results. Guo *et al.* fabricated carbon-coated MnO porous nanocomposites that exhibited enhanced electrochemical performance as anode materials.[32] Nagaraju *et al.* derived MnO@carbon composites from metal–organic frameworks (MOFs), achieving superior durability and cycling stability in lithium-ion batteries.[33] More recently, Wayu reviewed advances in MnO-carbon nanocomposites for energy storage applications, highlighting their potential in improving charge transport and structural stability.[34] These studies clearly demonstrate that integrating NiO or MnO nanoparticles within a carbon framework can significantly enhance electrochemical and functional properties, making such hybrid systems attractive for applications in sensors, batteries and supercapacitors. Nevertheless, the comparative influence of NiO and MnO nanoparticle incorporation on the electrical and dielectric characteristics of carbon materials remains insufficiently investigated.

In this work, a carbon matrix derived from the polymerization of pyrogallol-formaldehyde (CM) and its corresponding nanocomposites (CM/NiO and CM/MnO), obtained by incorporating NiO and MnO nanoparticles into the CM, were prepared using a sol–gel method. The main objective was to establish a correlation between structural disorder, charge transport and dielectric relaxation mechanisms. By comparing the respective effects of NiO and MnO incorporation, the present study sheds light on new insights into the role of transition metal oxides in tuning the electrical and dielectric properties of carbon-based materials for advanced electronic applications.

2. Experimental

2.1 Sample production

The carbon matrix (CM) was prepared through a three-step process, following the sol–gel method described by El Mir *et al.*[35,36] Pyrogallol (P) ($C_6H_3(OH)_3$;1,2,3-trihydroxybenzene; 97%; Fisher Scientific) was first solubilized in water (W) and then reacted with formaldehyde (F) (CH_2O; 99%; Biopharm) *via* catalysis by picric acid ($C_6H_3N_3O_7$;99%; Scharlau), using fixed P/F and P/W molar ratios of 1/3 and 1/6, respectively. The wet gel formed was aged and subsequently dried in a humid environment at 50 °C over two weeks, followed by controlled drying at 150 °C (10 °C per day) in a programmable oven, with a two-day isothermal hold to obtain the CM xerogel.

NiO and MnO nanoparticles were synthesized using $NiCl_2 \cdot 6H_2O$ (99.9% trace metals basis, Sigma-Aldrich) and $MnCl_2 \cdot 4H_2O$ (99.9% trace metals basis, Sigma-Aldrich) as precursors. 2 g of each precursor was solubilized in 14 ml of methanol (CH_3OH; 99.9%; Fisher Scientific), stirred for 15 min and then subjected to supercritical drying in ethanol ($T_c = 250$ °C, $P_c = 7$ MPa) using an autoclave. The obtained aerogels were calcined at 500 °C for 2 hours under atmospheric conditions in a muffle furnace.

The synthesized NiO and MnO nanoparticles were embedded in the CM matrix at a 5 wt% oxide/CM ratio. In the final step, the CM, CM/NiO and CM/MnO xerogels were pyrolyzed at 650 °C for 2 hours in a tubular furnace under a nitrogen gas flow. Prior to heating, the furnace was purged with nitrogen for five minutes to remove air from the chamber. Heating was then carried out under a nitrogen atmosphere to 650 °C with a controlled ramp rate of 5 °C min^{-1}, followed by conventional cooling to room temperature. For electrical measurements, the samples were prepared as monolithic parallelepipeds ($15 \times 6 \times 3$ mm^3), and silver paste was applied to two opposing faces to ensure good ohmic contact. The thickness was measured using a micrometer. The samples were placed in a liquid nitrogen cryostat, and impedance measurements were performed over a temperature range of 100–300 K with a 20 K step. At each temperature step, the system was allowed to stabilize until the temperature fluctuation was within ±0.5 K before recording the impedance data.

2.2 Characterization techniques

XRD patterns were recorded on a MiniFlex diffractometer equipped with a graphite monochromator using Co-Kα radiation. The morphology of the samples was investigated using field emission gun scanning electron microscopy (FEG-SEM, JSM-7600F). X-ray photoelectron spectroscopy (XPS) was performed using a Kratos AXIS Supra spectrometer with a monochromatic Al Kα source (1486.6 eV) to determine the surface composition and chemical states. The binding energies were calibrated using the C 1s peak of adventitious carbon at 284.5 eV, and charge compensation was achieved using a low-energy electron flood gun to minimize charging effects. Raman spectra were acquired with a Horiba Jobin-Yvon T64000 spectrometer using a 532 nm excitation laser. Dielectric and electrical properties were evaluated with an Agilent 4294A impedance analyzer applying a 50 mV excitation voltage.

3. Results and discussions

Fig. 1 shows the X-ray patterns of various samples. The XRD pattern of CM reveals an amorphous structure, characterized by two distinct broad bands at approximately 22° and 44°, attributed to the (002) and (100) crystallographic planes of graphite, respectively (JCPDS 29-0085).[37] In the CM/NiO nanocomposite, diffraction peaks at 44, 51 and 76° are attributed to the face-centered cubic (FCC) structure of metallic Ni, indexed to the (111), (200) and (220) planes (JCPDS 01-1260).[38] This indicates that NiO was reduced to metallic Ni during heat treatment at
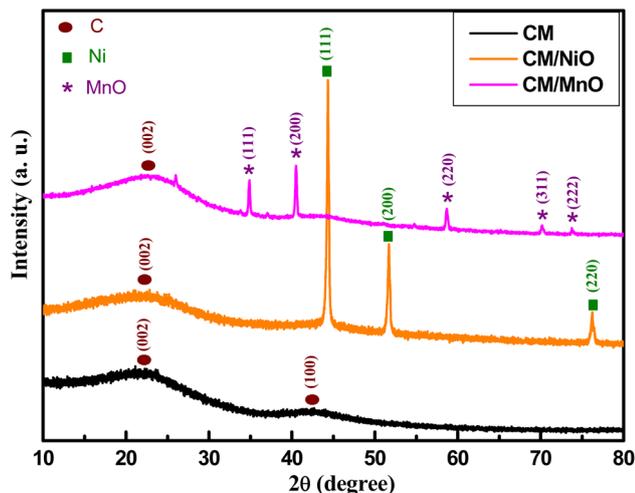
Fig. 1   . XRD patterns of CM, CM/NiO and CM/MnO.

650 °C. In the CM/MnO nanocomposite, peaks at 34°, 40°, 58°, 70° and 73° are attributed to cubic crystalline manganese monoxide MnO, assigned to the (111), (200), (220), (311) and (222) diffraction planes, respectively (JCPDS 07-0230).[39] In contrast to NiO, MnO (Mn^{2+}) remains thermally stable under identical conditions, resisting both reduction to metallic Mn (Mn^0) and oxidation to Mn^{3+}, due to its higher intrinsic stability.[40,41] It is also observed that the graphite band at 22° is present in both CM/NiO and CM/MnO nanocomposites, while the band at 44° disappears. The absence of this band can be attributed to overlap with the intense reflections of Ni and MnO phases in the nanocomposites. Furthermore, the much higher atomic diffusion of Ni and Mn compared to carbon makes the graphite contribution difficult to detect.[42,43]

Fig. 2 presents the SEM micrographs of various materials. The CM (image (a)) exhibits a porous texture with a disordered structure, which is advantageous for nanoparticle incorporation because of its extensive specific surface area and open framework. In the CM/NiO nanocomposite (image (b)), Ni nanoparticles are uniformly dispersed and well integrated into the carbon matrix, indicating strong interfacial interactions that facilitate efficient electron transfer and provide abundant active sites. The CM/NiO nanocomposite shows pocket-like regions that may facilitate electron pathways, enhancing conductance. By contrast, the CM/MnO nanocomposite (image (c)) exhibits long fiber-like structures and a less homogeneous distribution of MnO nanoparticles with evident agglomerates, which may decrease the specific surface area while increasing charge transport. These morphological characteristics demonstrate the significance of nanoparticle dispersion in governing the functional properties of pyrogallol-formaldehyde-based nanocomposites.
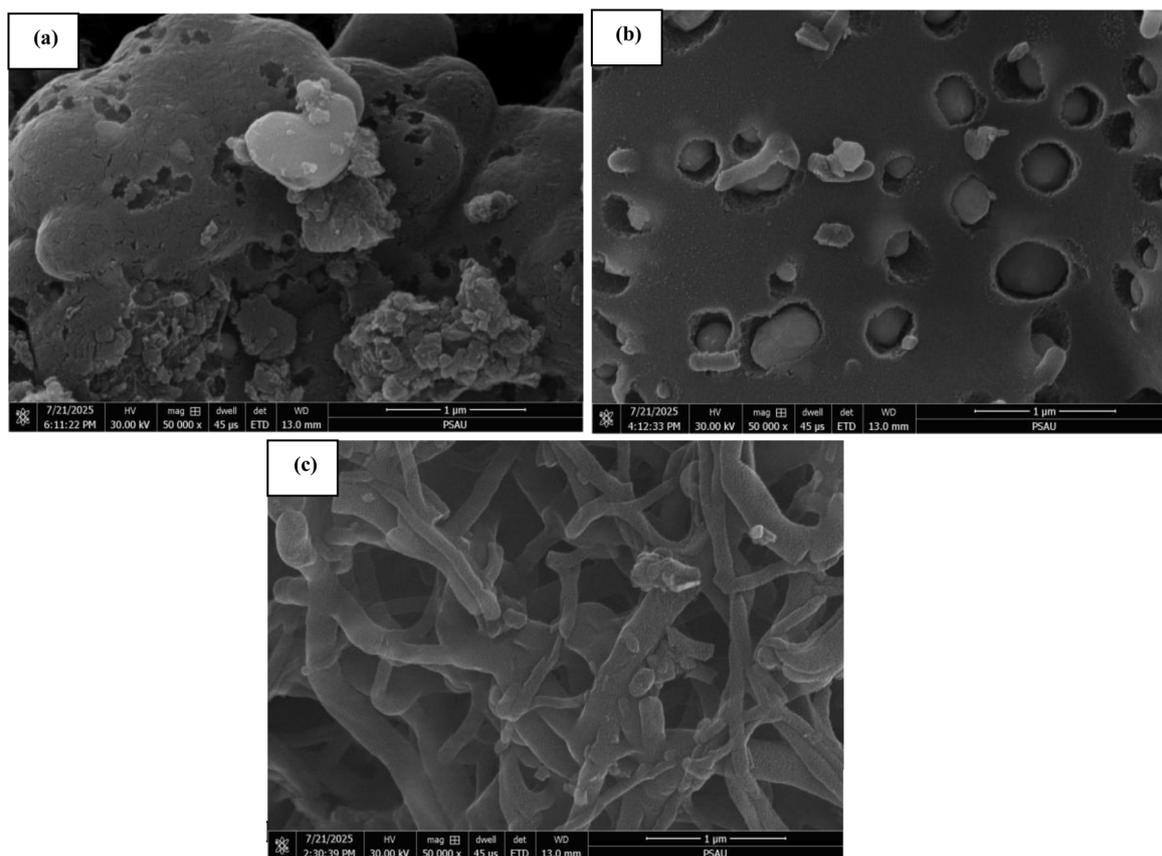

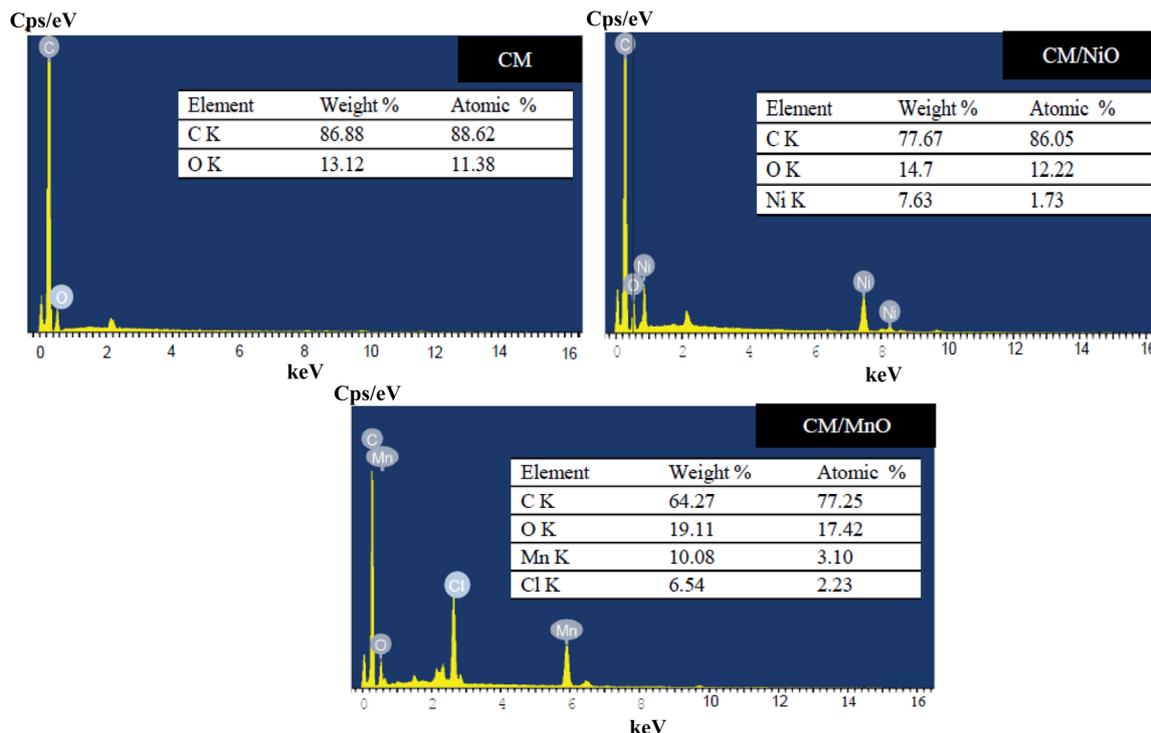Fig. 2   SEM micrographs of (a): CM, (b): CM/NiO and (c): CM/MnO.

Fig. 3 EDX patterns and elemental composition of different materials.

The chemical composition of the materials was examined using energy-dispersive X-ray spectroscopy (EDX) integrated with a scanning electron microscope. The mass and atomic percentages of oxygen, carbon, nickel, manganese and chlorine in different samples are summarized in the tables of Fig. 3. Notably, chlorine is detected only in the CM/MnO nanocomposite, despite both NiO and MnO precursors containing chlorine ($NiCl_2 \cdot 6H_2O$ for NiO and $MnCl_2 \cdot 4H_2O$ for MnO). This observation is consistent with the XRD results. Specifically, the presence of metallic Ni in the Carbon/NiO hybrid nanocomposite indicates the partial reduction of Ni^{2+} to Ni^0 by the carbon matrix, promoting the release and elimination of chlorinated species. In contrast, manganese remains predominantly as MnO, which facilitates the retention of chlorinated residues or the formation of stable oxychlorides detectable by EDX.

Fig. 4 shows the XPS spectra of different samples. A C 1s peak at approximately 284 eV, typical of carbon, accompanied by a weak O 1s signal indicating the presence of oxygenated functional groups, is observed in all samples. XPS analysis of the C/NiO nanocomposite shows Ni 3p peaks at around 68 eV and a Ni 2p peak at 855 eV, consistent with surface-oxidized Ni species. Bulk XRD measurements reveal the formation of metallic Ni nanoparticles, which are primarily responsible for the conductive properties of the nanocomposite. For the CM/MnO nanocomposite, the Mn 3p peak at approximately 49 eV, together with the Mn 2p peaks at around 642 eV and 654 eV, confirms the presence of manganese in its oxidized form, characteristic of MnO. Additionally, the presence of chlorine in the CM/MnO nanocomposite, detected by EDX analysis, is confirmed by XPS, as indicated by two peaks at approximately 200 eV and 270 eV, corresponding to Cl 2p and Cl 2s, respectively.

Table 1 displays the atomic concentrations of detected elements. The CM consists mainly of carbon (87 at%) and surface oxygen (13 at%). In the CM/NiO nanocomposite, nickel is detected at 1.7 at% with a slight reduction in oxygen, confirming the incorporation of NiO. For CM/MnO, the carbon content decreases (82 at%), while manganese reaches 2.7 at%, and chlorine (3 at%) is observed, likely originating from the
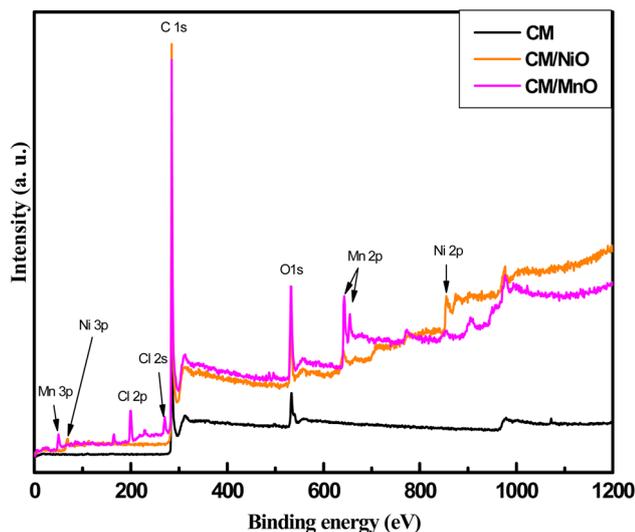

Fig. 4 XPS measurements of various samples.

Paper

Table 1 Atomic concentrations of detected elements obtained from XPS analysis for the various materials

Cl (at%)	Mn (at%)	Ni (at%)	O (at%)	C (at%)	Material
—	—	—	12.94	87.05	CM
—	—	1.73	10.14	88.12	CM/NiO
3.03	2.71	—	12.59	81.66	CM/MnO

$MnCl_2$ precursor. These findings confirm the successful integration of metal oxides and their influence on the surface composition.

Fig. 5 presents the high-resolution XPS spectra of CM, CM/NiO and CM/MnO. The C 1s spectra of all samples exhibit a single peak centered at 284.5 eV, corresponding to C–C/C=C bonds, indicating that the carbon framework remains largely preserved after metal oxide incorporation. The O 1s spectrum of the CM sample exhibits a main component centered at 532.4 eV, which can be assigned to surface oxygen species, such as C–O bonds and hydroxyl groups, while the weak feature observed around 538.8 eV is attributed to a background contribution. In contrast, the O 1s spectra of CM/NiO and CM/MnO nanocomposites display a single component at 531.5 eV,
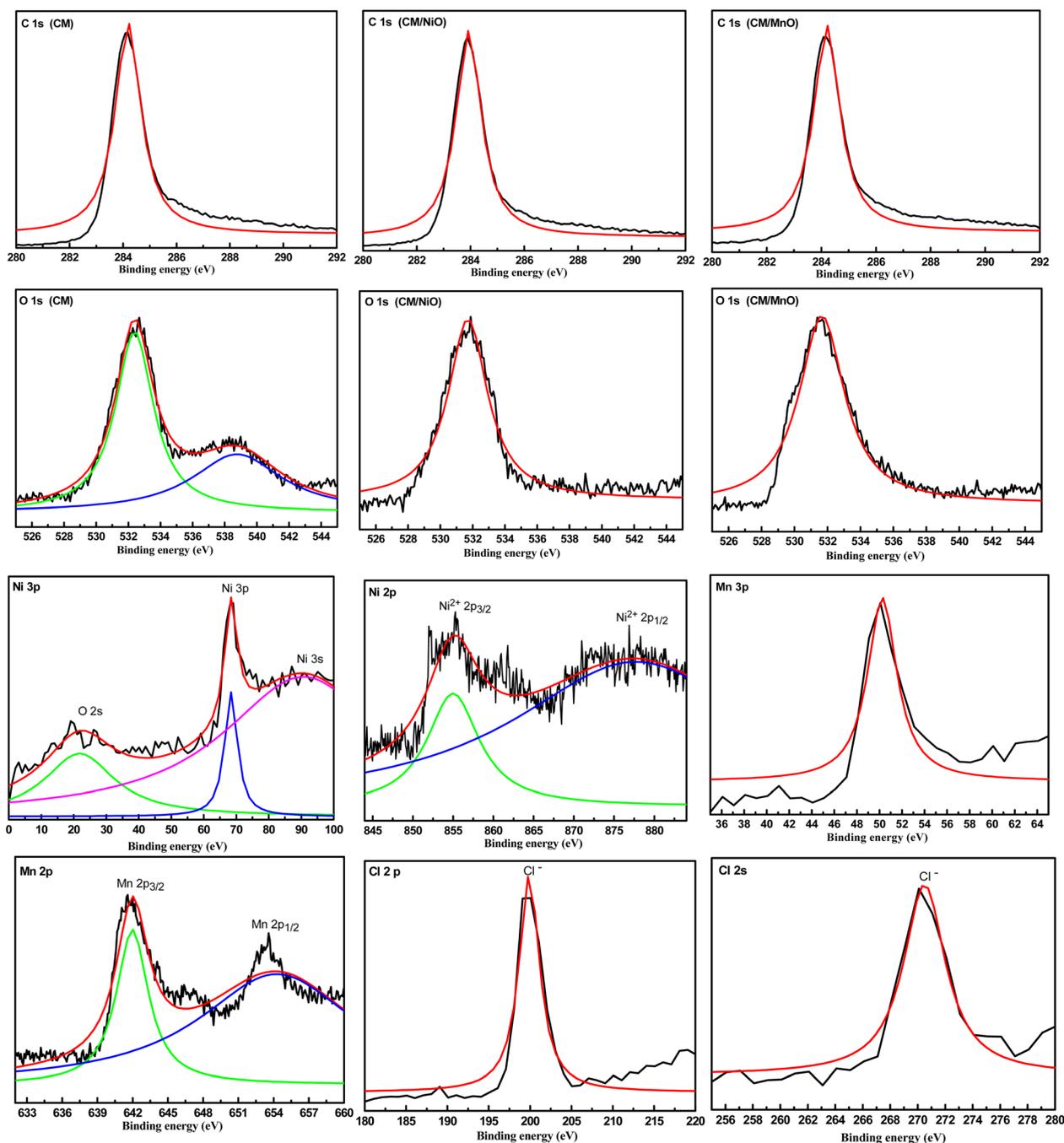
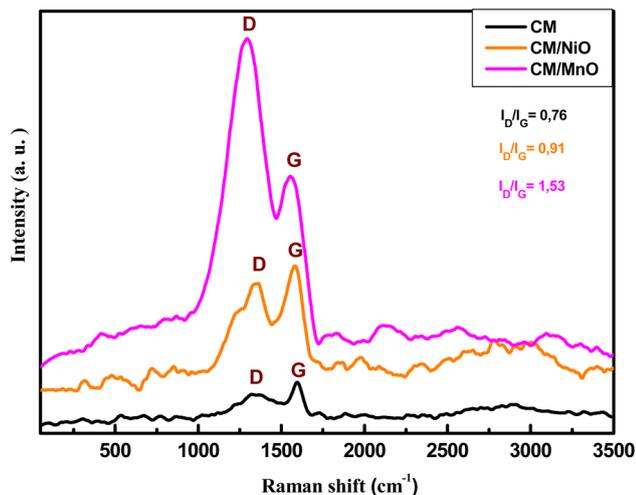**Fig. 5** High-resolution XPS spectra of CM, CM/NiO and CM/MnO.

Fig. 6 Raman analysis of different samples, highlighting the D and G peaks and their corresponding I_D/I_G intensity ratios.

Fig. 8 Arrhenius plots of DC conductivity *versus* 1000/T for various samples.

corresponding to surface oxygen species and interfacial oxygen (O–C–M), indicating the presence of oxygen-containing groups at the carbon/metal oxide interface. In the CM/NiO sample, the
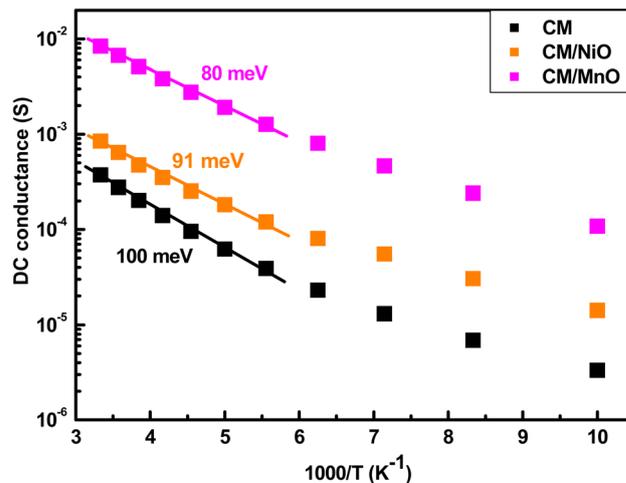
peaks at 21.8 and 90.7 eV are assigned to O 2s and Ni 3s states, respectively, while the Ni 3p signal at 68.4 eV confirms the presence of nickel oxide within the carbon matrix. The Ni 2p
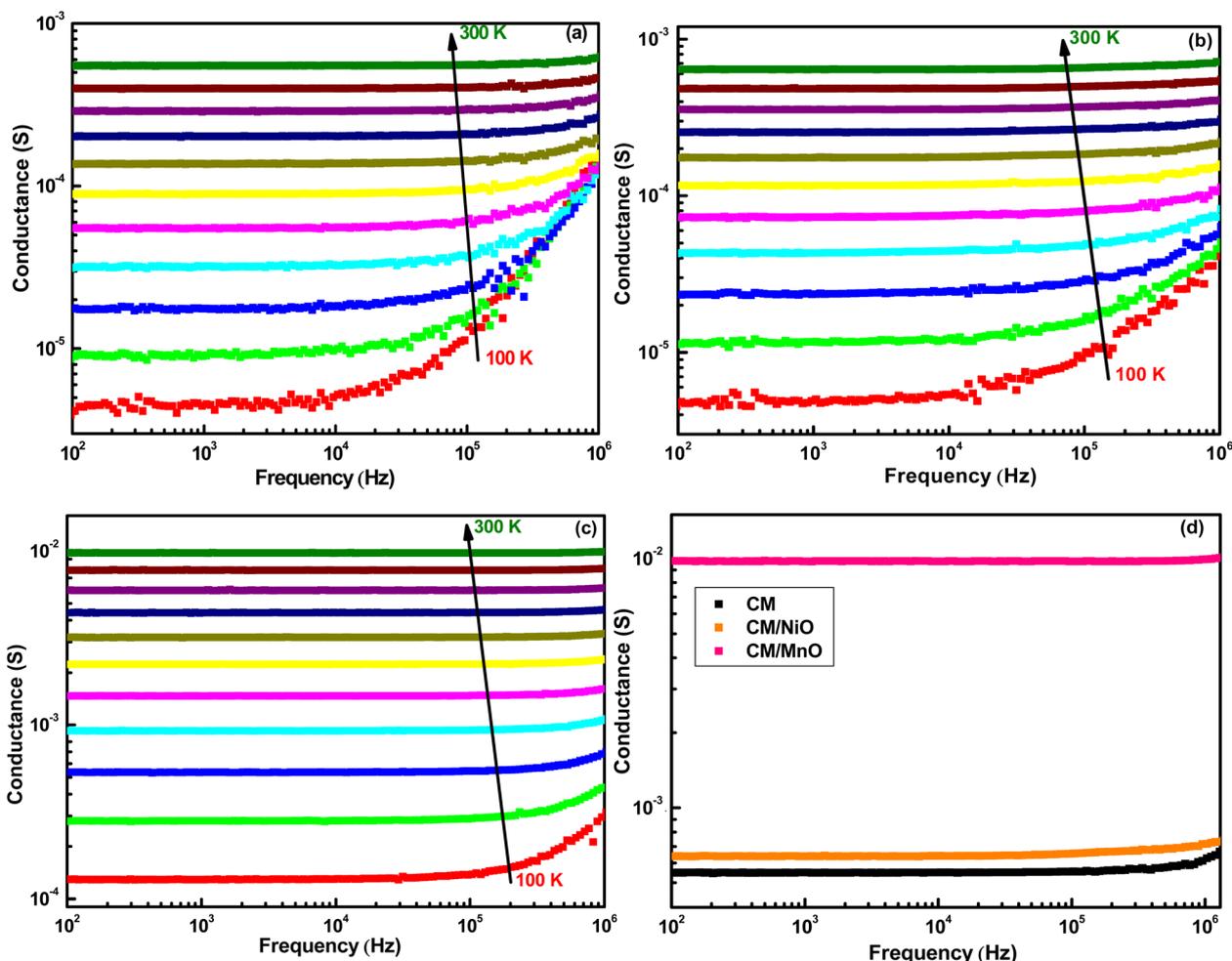

Fig. 7 AC conductance at various measurement temperatures with a step of 20 K for (a): CM, (b): CM/NiO, (c): CM/MnO and (d): at room temperature.
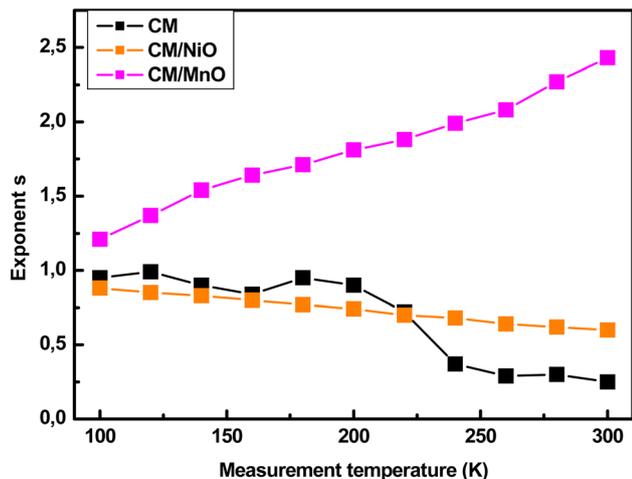
Fig. 9 Dependence of the frequency exponents on temperature for various samples.

Table 2 Equivalent circuit parameters (R and Q) obtained from impedance fitting for different samples

Q (10^{-10} F)			R (kΩ)			
CM/MnO	CM/NiO	CM	CM/MnO	CM/NiO	CM	T (K)
5.40	2.59	3.40	73	205	1839	100
4.99	2.64	3.75	17	42	324	140
4.80	2.68	4.10	5.3	13.5	86.1	180
4.73	2.72	4.27	3.3	8.5	49.3	200
4.32	2.93	4.66	1.4	3.9	19.1	240
3.79	3.73	4.82	0.5	1.5	6.2	300

at 642 eV (Mn $2p_{3/2}$) and 654.3 eV (Mn $2p_{1/2}$), characteristic of manganese oxide (Mn^{2+}/Mn^{3+}). The Mn 3p peak at 50.2 eV further confirms the presence of Mn in this nanocomposite. Finally, Cl 2p and Cl 2s peaks at 200 eV and 270.5 eV indicate residual chloride species (Cl$^-$) originating from the precursor salts used during the synthesis of the CM/MnO nanocomposite.

The Raman signals of CM, CM/NiO and CM/MnO materials in Fig. 6 show two distinctive carbon peaks: the D peak around 1350 cm^{-1}, related to lattice defects and disruptions in the sp^3

spectrum shows a main Ni $2p_{3/2}$ peak at 855 eV (Ni^{2+}) and a characteristic satellite at 877.7 eV, which is typical of NiO. For the CM/MnO nanocomposite, the Mn 2p spectrum shows peaks
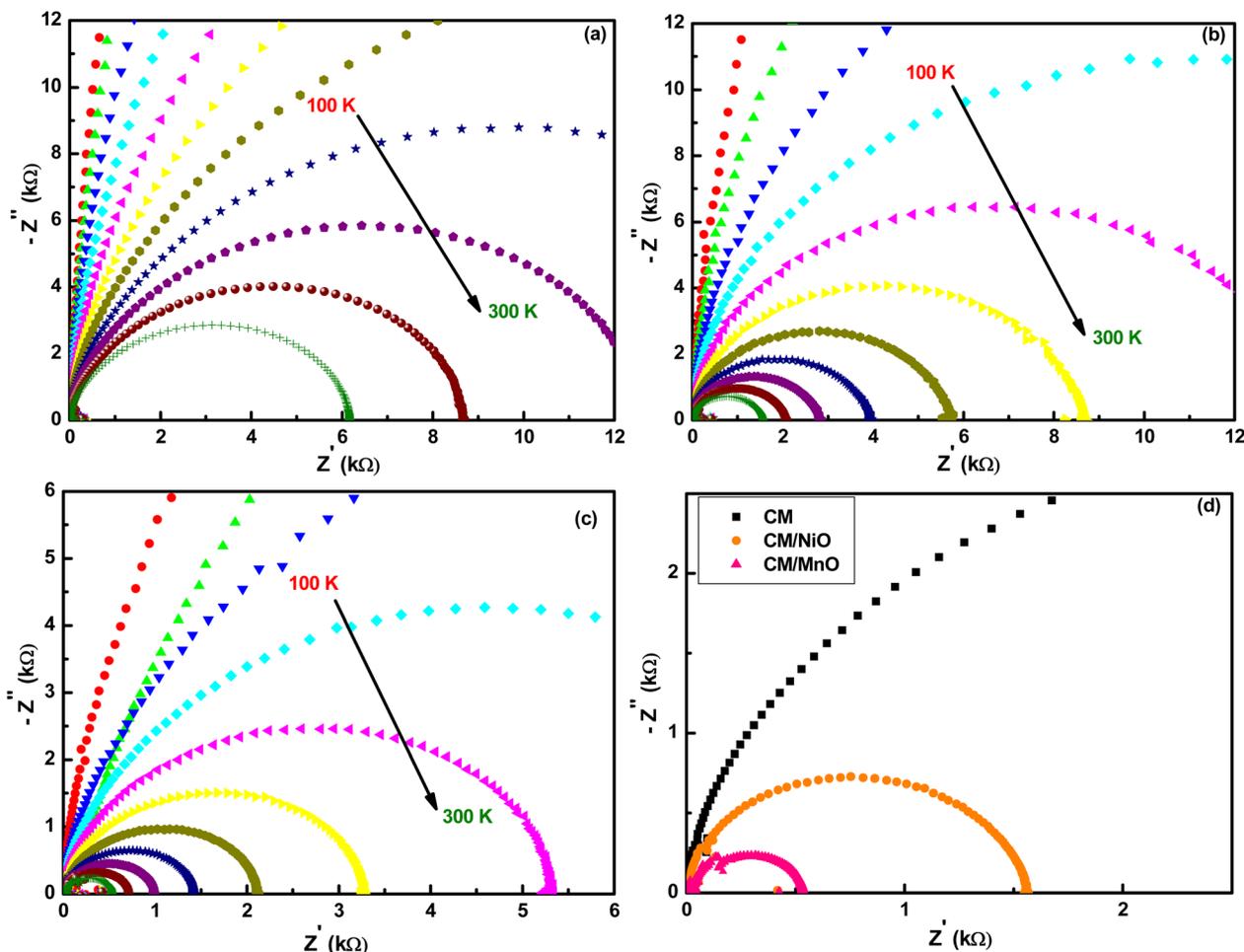

Fig. 10 Nyquist plots at various measurement temperatures with a step of 20 K for (a): CM, (b): CM/NiO, (c): CM/MnO and (d): at room temperature.

network and the G peak near 1580 cm^{-1}, corresponding to the E$_2$g vibrational mode of sp^2 carbon atoms in graphitic regions. The intensity ratio I_D/I_G provides a measure of structural disorder: 0.76 for CM, indicating a relatively ordered structure; 0.91 for CM/NiO, suggesting a slight increase in defects, and 1.53 for CM/MnO, pointing to pronounced disorder and significant fragmentation of graphitic domains. This trend demonstrates that MnO incorporation considerably increases defect density in the carbon matrix, further enhanced by the presence of trace chlorine detected exclusively in CM/MnO, which may contribute to the creation of active sites and facilitate charge transport.

To investigate the influence of NiO and MnO on the electrical conductivity of the carbon matrix, conductance measurements were performed in the AC regime at temperatures between 100 K and room temperature, as illustrated in Fig. 7. The rise in conductance with both temperature and frequency confirms the semiconducting nature of the materials. Among the samples, the CM/MnO nanocomposite exhibits the highest conductance, while CM shows the lowest values across all measurement temperatures, particularly at 300 K (Fig. 7d). The superior conductance of the CM/MnO nanocomposite can be attributed to several factors. First, the addition of MnO nanoparticles to the carbon matrix introduces numerous structural defects and

enhances interfacial interactions, thereby increasing the density of charge carriers. In addition, manganese oxides possess multiple oxidation states (Mn^{2+}/Mn^{3+}), which promote charge transport *via* hopping mechanisms. Trace amounts of chlorine introduce supplementary defect states that slightly facilitate carrier hopping, contributing modestly to the enhanced conductance observed in CM/MnO. In contrast, the CM sample exhibits the lowest conductance because of its amorphous and highly porous nature, which significantly restricts electronic transport.[44–46] The CM/NiO nanocomposite exhibits an intermediate electrical conductance mainly governed by the presence of metallic Ni detected by XRD, which provides primary conductive pathways within the composite. XPS analysis reveals residual oxidized Ni species (NiO) confined to the surface, whose direct contribution to bulk electrical conductivity is expected to be limited. While the partial reduction of NiO to metallic Ni enhances charge transport, the remaining surface NiO may introduce localized interfacial barriers rather than controlling the overall conduction. Furthermore, the porous and disordered structure of the carbon matrix, together with incomplete percolation of metallic Ni domains, hinders the formation of continuous electron transport networks, resulting in the observed intermediate conductance behavior.[47,48] The variation in conductance is consistent
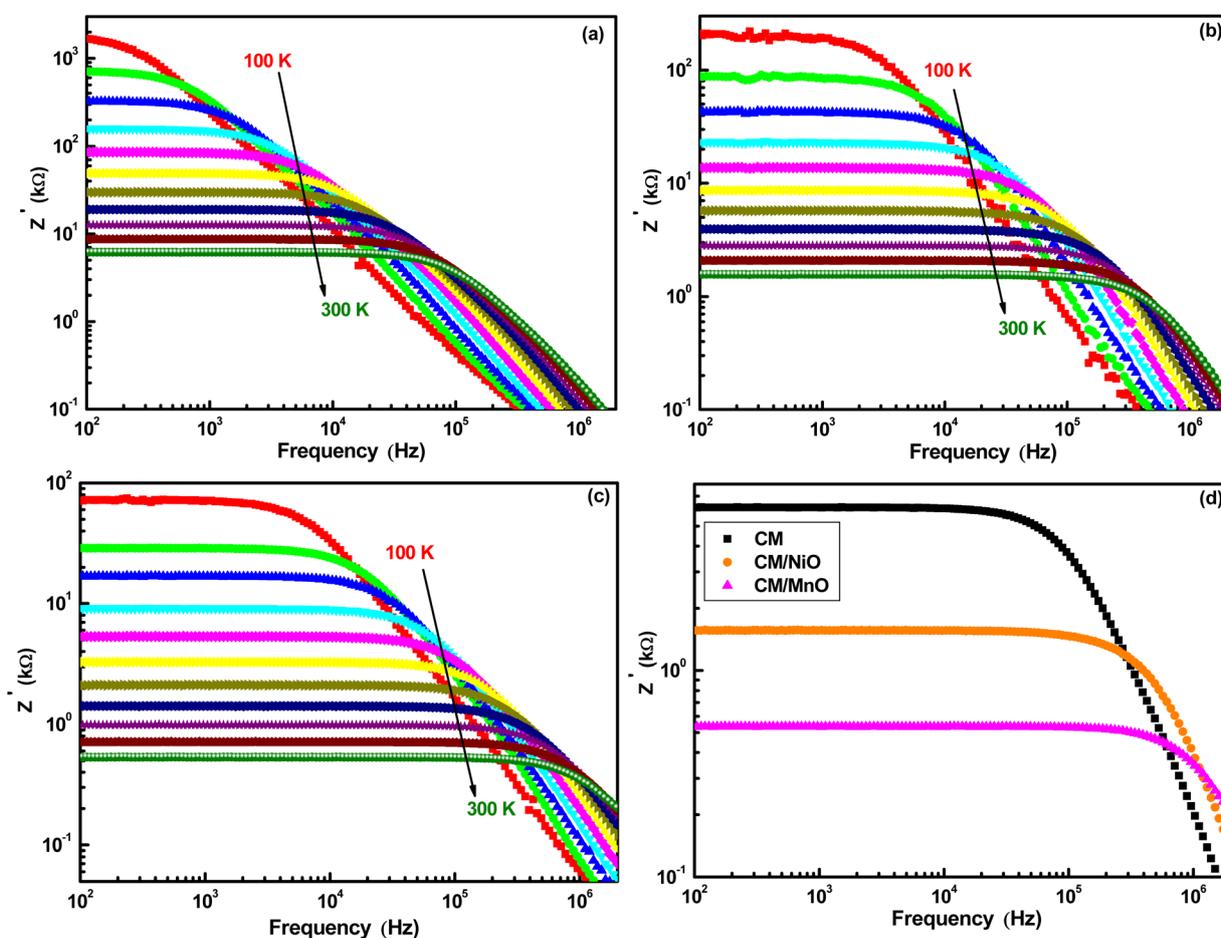

Fig. 11 Dependence of the real component of impedance (Z') with frequency at various measurement temperatures with a step of 20 K for (a): CM, (b): CM/NiO, (c): CM/MnO and (d): at room temperature.
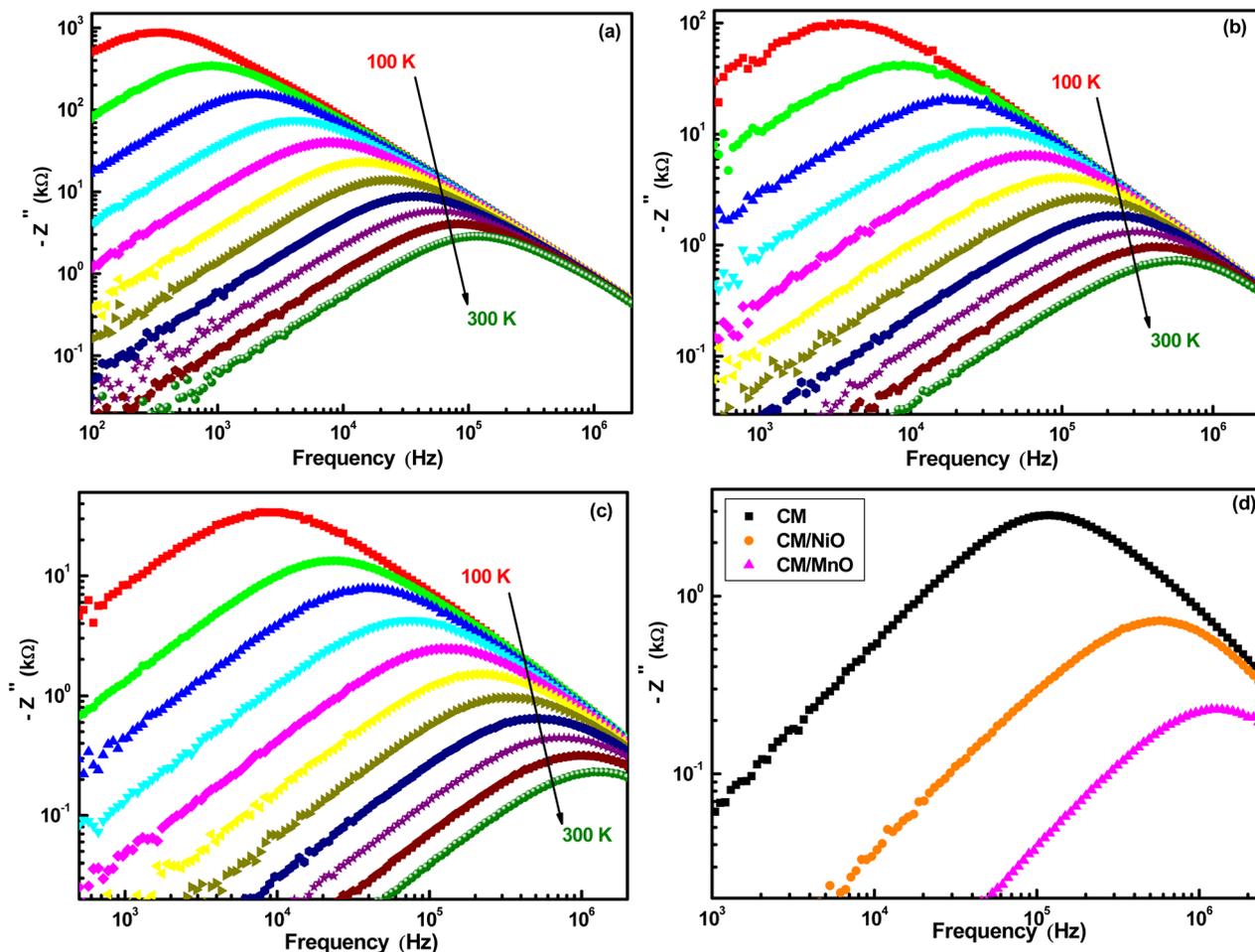
Fig. 12 Dependence of the opposite imaginary component of impedance ($-Z''$) with frequency at various measurement temperatures with a step of 20 K for (a): CM, (b): CM/NiO, (c): CM/MnO and (d): at room temperature.

with the I_D/I_G ratios obtained from Raman spectroscopy (0.76 for CM, 0.91 for CM/NiO and 1.53 for CM/MnO). In fact, the higher disorder in CM/MnO increases the number of localized sites, which facilitates charge transport and explains its higher conductivity compared to CM and CM/NiO.

Fig. 8 depicts the dependence of DC conductance (in the low frequency region) on the reciprocal of the measurement temperature. The observed behavior indicates that the DC conductance obeys the Arrhenius law:[49]

$$G_{dc} = G_0 \, \exp\left(\frac{E_a}{k_B T}\right) \tag{1}$$

G_0 is the pre-exponential factor, E_a is the activation energy, k_B is the Boltzmann constant, and T is the measurement temperature.

The calculated activation energies at high temperatures are approximately 100 meV for CM, 91 meV for the CM/NiO nanocomposite and 80 meV for the CM/MnO nanocomposite. The progressive decrease in the activation energy suggests that the integration of NiO and MnO into the carbon framework enhances charge transport. In the CM/NiO material, the presence of metallic nickel provides additional conduction pathways, facilitating electron mobility. In CM/MnO, the

combination of MnO and trace chlorine introduces additional active sites and multiple oxidation states, which further promote charge carrier hopping and reduce the energy barrier for conduction.
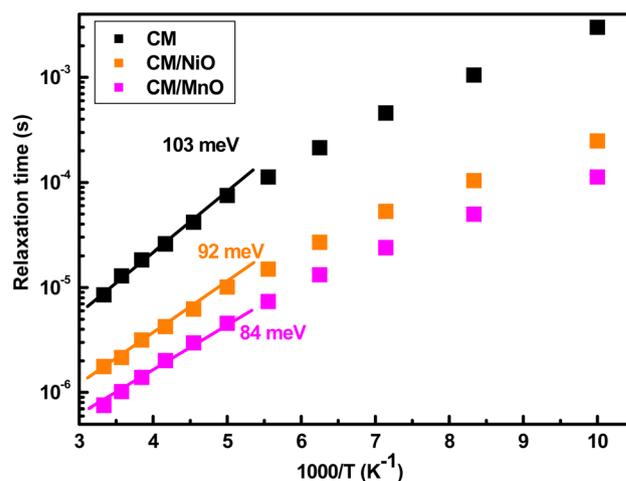

Fig. 13 Arrhenius representation of relaxation time *versus* 1000/T for different samples.

The frequency dependence of AC conductance for the samples follows the Jonscher universal power law:[50]

$$G_{AC}(\omega) = G_{DC} + A\omega^s \tag{2}$$

A is the pre-exponential factor, ω is the angular frequency and s is the frequency exponent, providing information on the conduction mechanism.

The exponent s, extracted from the fit using eqn (2) (Fig. 9), shows distinct conduction mechanisms for the different samples. In CM, the exponent s ranges from 0 to 1, indicating general charge carrier hopping between localized states.[51] For the CM/NiO nanocomposite, s decreases with increasing temperature, suggesting that conduction is dominated by correlated barrier hopping (CBH) due to metallic nickel, facilitating charge transport.[52] In contrast, for the CM/MnO nanocomposite, s increases with temperature, indicating thermally activated small polaron hopping (SPH), assisted by manganese oxidation states.[53]

Fig. 10 presents the Nyquist diagrams of different materials over the temperature range of 100–300 K. In fact, the Nyquist diagram represents the complex electrical impedance of the material, where the imaginary part ($-Z''$) is plotted *versus* the real part (Z'). In these samples, the grains (regions of high conductivity) and grain boundaries (regions between adjacent grains) play a role in the overall impedance. In this case, the diagrams exhibit a single depressed semicircular arc at all measurement temperatures, indicating a single relaxation process predominantly associated with the grain boundary response. The progressive reduction in arc radius with rising temperature reflects the thermally activated nature of the relaxation process. The Nyquist arc radius decreases from CM to CM/NiO to CM/MnO (Fig. 10d), indicating a progressive reduction in resistance and enhanced charge transport, associated with the impact of Ni nanoparticles in the CM/NiO nanocomposite and Mn^{2+}/Mn^{3+}-assisted polaron hopping in the CM/MnO nanocomposite.

The impedance data of our samples were adjusted using the same equivalent circuit, composed of two parallel elements: a resistor (R) and a constant phase element (CPE). The impedance of the CPE is given by:[54]

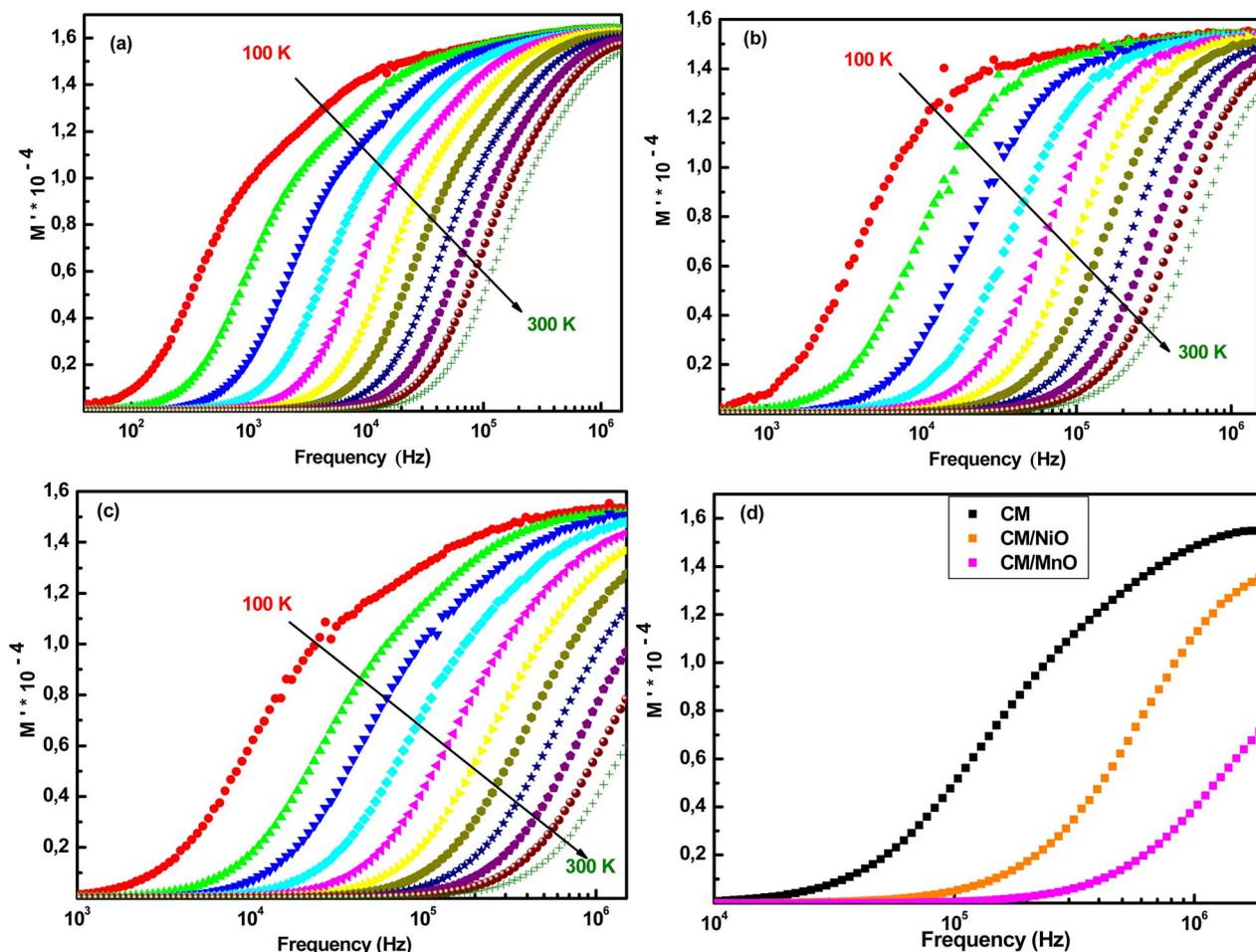$$Z_{CPE} = \frac{1}{Q(i\omega)^\alpha} \tag{3}$$

Fig. 14 Dependence of the real component of modulus M' with frequency at various measurement temperatures with a step of 20 K for (a): CM, (b): CM/NiO, (c): CM/MnO and (d): at room temperature.

Here, i is the imaginary unit, Q is defined in $\Omega^{-1}s^{\alpha}$ and α is a constant ranging from 0 to 1 (0 for purely resistive behavior and 1 for ideal capacitive behavior).

The parameters of the equivalent circuit (R and Q) are reported in Table 2. It is clear that the CPE element behaves like a capacitor, as the value of α was found to be close to 1. It is also noted that the grain boundary resistance (R) of different materials decreases with increasing temperature, suggesting that the thermally activated transport of localized charge carriers enhances their mobility, thereby promoting more efficient hopping conduction and reducing resistive behavior. In contrast, the grain boundary capacitance (Q) increases with temperature for both CM and the CM/NiO nanocomposite, which can be attributed to thermally activated charge carriers enhancing interfacial polarization and dipole reorientation. Conversely, in the CM/MnO nanocomposite, Q decreases with temperature, likely due to diminished interfacial polarization and the recombination of thermally activated carriers associated with the Mn^{2+}/Mn^{3+} mixed valence states. At higher temperatures, this leads to a more dominant conductive behavior, further supported by residual chlorine, which introduces additional localized defects that slightly reduce capacitive effects.

Fig. 11 depicts the variation of the real component of the complex impedance (Z') with frequency at different temperatures. Two separate regions can be observed: the first, which is frequency-independent at low frequencies, corresponds to DC conductance arising from the long-range motion of charge carriers. In contrast, the second region, which is frequency-dependent at high frequencies, is associated with AC conductance resulting from short-range localized charge carrier motion. The high Z' values at low frequencies and low temperatures, which tend to decrease with increasing temperature, indicate that the materials exhibit a negative temperature coefficient of resistance, confirming their semiconducting nature. The convergence of Z' curves at high frequencies further suggests the presence of a space charge region. At room temperature (Fig. 11d), the decrease in Z' from CM to CM/NiO and further to CM/MnO can be attributed to enhanced charge transport resulting from the incorporation of metal oxides. This improvement in electrical conductance arises from the combined interaction between the carbon matrix and inorganic nanoparticles.

The spectra of the opposite imaginary component of impedance ($-Z''$) (Fig. 12) exhibit an initial increase with frequency at every temperature, attaining a maximum at the relaxation frequency f_{max} and then decreasing at frequencies above f_{max}. The relaxation peaks are pronounced, wide and non-symmetric, indicating non-Debye type behavior. The increase in f_{max} with temperature indicates the existence of a thermally activated relaxation process. The observed overlap of Z'' at high frequencies suggests that space charge polarization occurs only
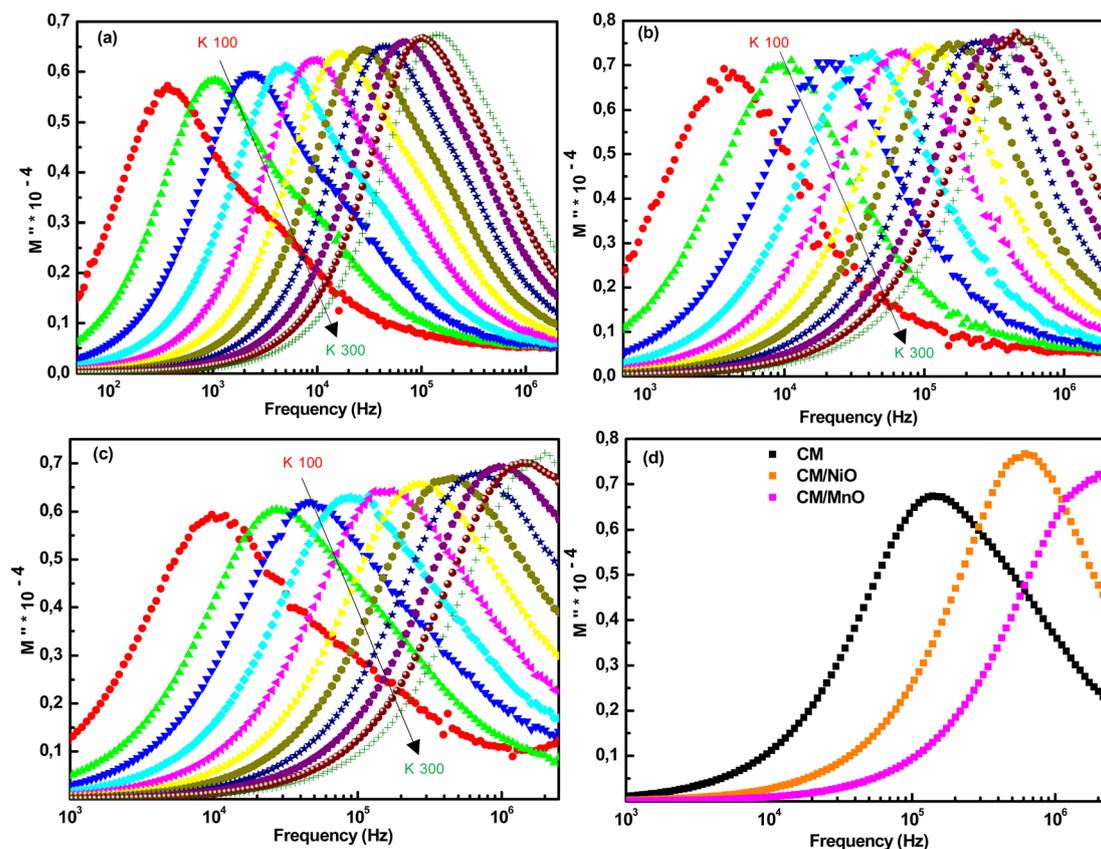

Fig. 15 Dependence of the imaginary component of modulus M'' with frequency at various measurement temperatures with a step of 20 K for (a): CM, (b): CM/NiO, (c): CM/MnO and (d): at room temperature.

at low frequencies. Therefore, the materials polarize for $f < f_{max}$ and relax for $f > f_{max}$. At room temperature (Fig. 12d), CM, being the most insulating, relaxes at lower frequencies, while CM/NiO relaxes at intermediate frequencies and CM/MnO, the most conductive, relaxes at higher frequencies. This behavior reflects the fact that the more conductive a material is, the faster its charges can respond to the applied AC field, shifting the Z'' peak toward higher frequencies. Conversely, in more insulating materials, charge relaxation is slower, causing the peak to appear at lower frequencies.

Fig. 13 illustrates the evolution of the relaxation time ($1/f_{max}$) with 1000/T for different samples. The relaxation time decreases with increasing conductivity and temperature, reflecting faster charge transport in the materials. CM, being the most insulating, exhibits the longest relaxation time, while CM/NiO and CM/MnO nanocomposites show progressively shorter relaxation times due to their higher conductivities.

The calculated activation energies are approximately 103 meV for CM, 92 meV for the CM/NiO nanocomposite and 84 meV for the CM/MnO nanocomposite. These values are close to the activation energies obtained in the DC regime (100 meV for CM, 91 meV for CM/NiO and 80 meV for CM/MnO), confirming the proportionality between DC conductance and relaxation time and indicating that a similar conduction mechanism governs both DC and AC regimes.

In order to reduce electrode polarization effects at low frequencies and highlight the relaxation phenomena within the material bulk, the analysis was further carried out using the electrical modulus (M^*) representation, which can be written as:

$$M^* = j\omega C_0 Z^* = M' + jM'' \tag{4}$$

C_0 is determined from the following relation:

$$C_0 = \frac{\varepsilon_0 S_e}{e} \tag{5}$$

Here, ε_0 is the permittivity of free space (8854×10^{-12} F m^{-1}), S_e is the electrode area and e is the material thickness. Fig. 14 illustrates the dependence of the real component of the complex modulus (M') at various temperatures. It is evident that, at all temperatures, M' approaches zero at low frequencies, reflecting the minimal contribution of electrode polarization. With increasing frequency, M' rises steadily, which can be attributed to conduction mechanisms related to the charge carriers short range.

At room temperature (Fig. 14d), all samples display similar frequency-dependent behavior. Nevertheless, the CM/MnO nanocomposite exhibits slightly higher M' values than CM and CM/NiO, indicating enhanced local charge carrier mobility and modified relaxation dynamics due to the incorporation of
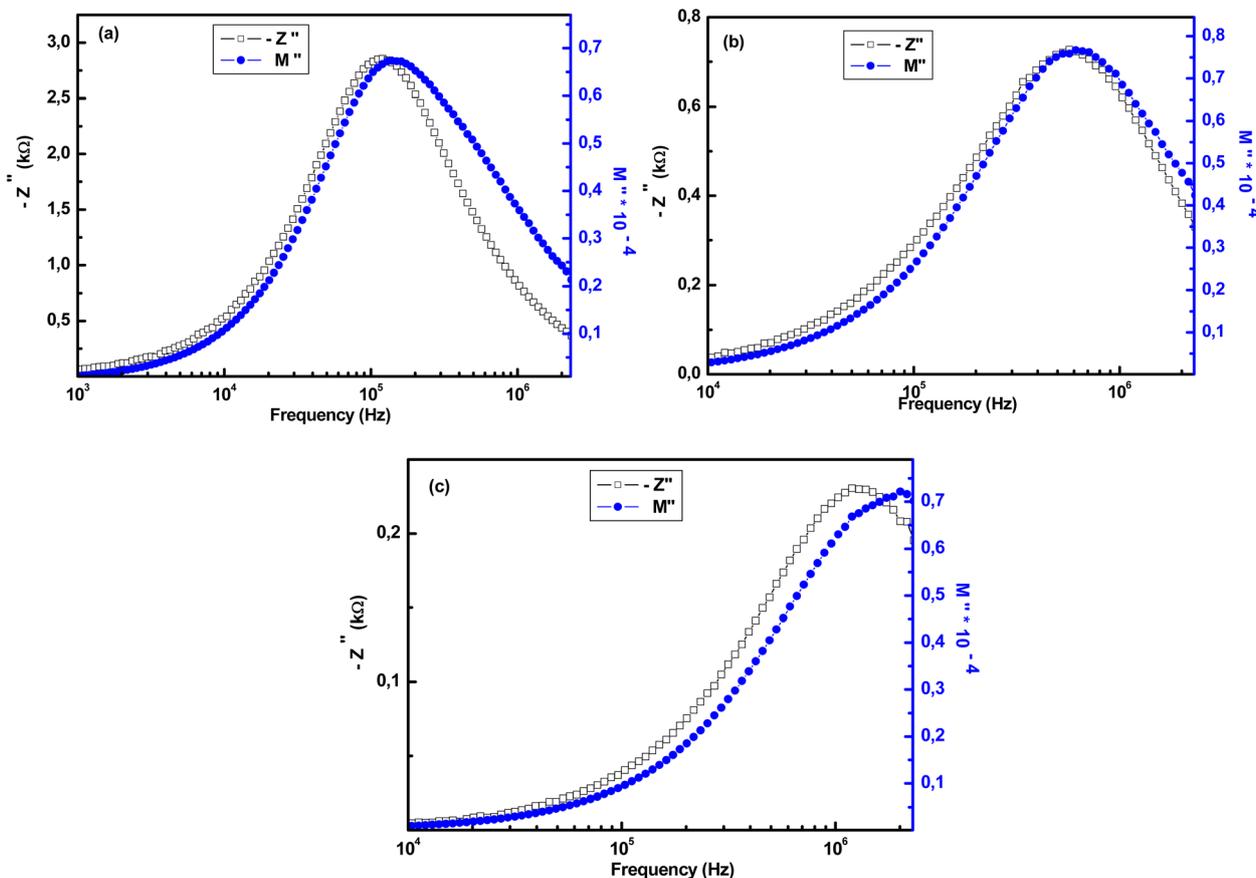

Fig. 16 The variation of the opposite imaginary component of impedance ($-Z''$) and the imaginary component of electric modulus (M'') at room temperature for the (a): CM, (b): CM/NiO, and (c): CM/MnO samples.

MnO nanoparticles. This behavior is further supported by the presence of residual chlorine, which introduces localized defects that contribute to short-range charge motion. These findings highlight the significant influence of metal oxide nanoparticles together with chlorine-related defect states on the dielectric response of CM.

Fig. 15 illustrates the dependence of the imaginary component of complex modulus (M'') at various temperatures. The absence of peaks at low frequencies indicates long-range charge carrier mobility, whereas the peaks observed at higher frequencies are associated with localized charge motion.[55–57] Upon increasing the temperature, the relaxation peaks shift to higher frequencies, indicating that the relaxation process is governed by thermal activation.

At room temperature (Fig. 15d), all samples display similar responses of M'', suggesting comparable relaxation dynamics. However, the relaxation frequency is the highest for the CM/MnO nanocomposite, intermediate for CM/NiO and the lowest for CM. This trend indicates that the incorporation of conductive inorganic nanoparticles, such as NiO and MnO, enhances local charge carrier mobility and facilitates charge hopping between sites. In contrast, the absence of such inorganic nanoparticles increases interfacial resistance and impedes charge transport, resulting in slower relaxation dynamics. Finally, the asymmetry of the observed peaks points to a non-Debye relaxation behavior, associated with a distribution of relaxation times arising from structural or compositional heterogeneities within the materials.

To gain a deeper understanding of the relaxation and conduction mechanisms, the frequency dependence of the imaginary parts of impedance ($-Z''$) and electric modulus (M'') was examined at room temperature (Fig. 16). The well-defined relaxation peaks observed in both plots confirm that charge carriers undergo localized relaxation rather than long range transport, consistent with a short range hopping mechanism. The shift of these peaks toward higher frequencies for CM/NiO and CM/MnO nanocomposites reveals shorter relaxation times and enhanced carrier mobility. This suggests that the incorporation of NiO and MnO nanoparticles facilitates localized conduction by introducing additional hopping centers and reducing potential barriers. Overall, electrical conduction in all
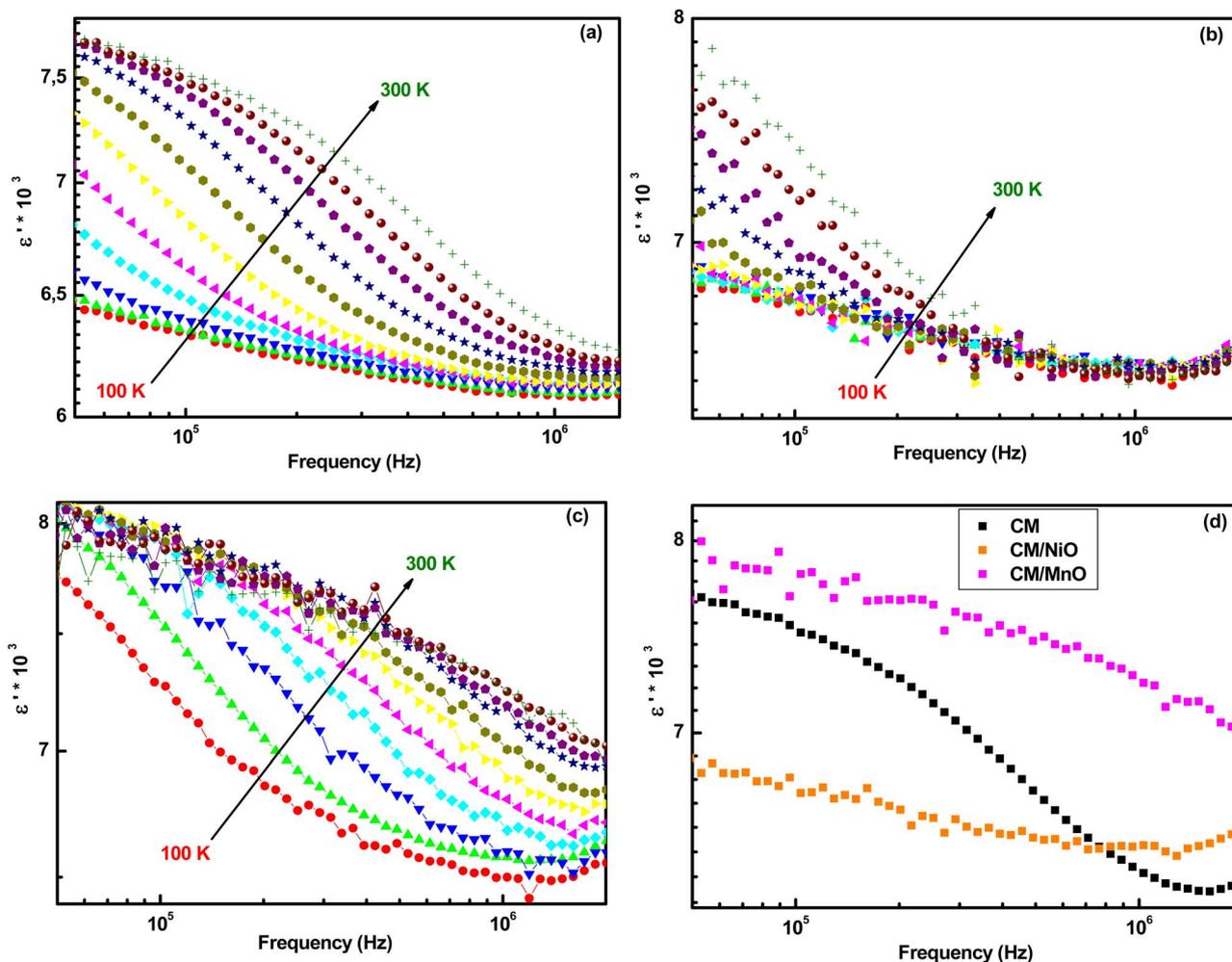

Fig. 17 Frequency dependence of the real component of permittivity (ε') for (a): CM, (b): CM/NiO, and (c): CM/MnO at different measurement temperatures with a step of 20 K and (d): at room temperature.

samples is mainly governed by a hopping-type process, with improved charge dynamics upon metal oxide incorporation.

To determine the nature of the dielectric polarization, the complex dielectric permittivity of the material was investigated and can be calculated using the following equation:

$$\varepsilon = \varepsilon' + j\varepsilon'' = \frac{1}{j\omega C_0 Z^*} \qquad (6)$$

The variation of the real component of permittivity (ε') with increasing frequency and temperature for CM, CM/NiO and CM/MnO samples is presented in Fig. 17. ε' exhibits a pronounced decrease as the frequency increases, which is characteristic of Maxwell–Wagner interfacial polarization. As the temperature increases, ε' rises for all samples, reflecting the thermal activation of charge carriers.

At room temperature (Fig. 17d), the CM/MnO nanocomposite exhibits the highest permittivity, indicating a more efficient interfacial polarization process. This behavior can be attributed to local Mn^{2+}/Mn^{3+} electronic transitions and the homogeneous dispersion of MnO nanoparticles, both of which enhance the density of active interfacial sites. In contrast, the

CM/NiO nanocomposite shows a lower ε' value at room temperature, likely due to the conductive contribution of metallic Ni. The presence of Ni nanoparticles enhances charge transport, which can lead to increased charge leakage and a reduced capacitive response of the material. These observations confirm that the dielectric response of the studied composites follows a non-Debye relaxation behavior, predominantly controlled by Maxwell–Wagner-type interfacial polarization.

Fig. 18 presents the variation of the imaginary component of permittivity (ε'') with increasing frequency and temperature for CM, CM/NiO and CM/MnO samples. A clear reduction in ε'' with increasing frequency is observed, which is characteristic of a loss mechanism governed by conduction and interfacial polarization. At room temperature (Fig. 18d), the CM/MnO nanocomposite exhibits the highest ε'' value, indicating a significant contribution from local Mn^{2+}/Mn^{3+} electronic transitions and enhanced interfacial polarization. The residual chlorine generates localized defect states that reinforce short-range interfacial polarization, thereby influencing the dielectric loss behavior of CM/MnO. In contrast, the CM/NiO nanocomposite exhibits low dielectric losses at low temperatures,
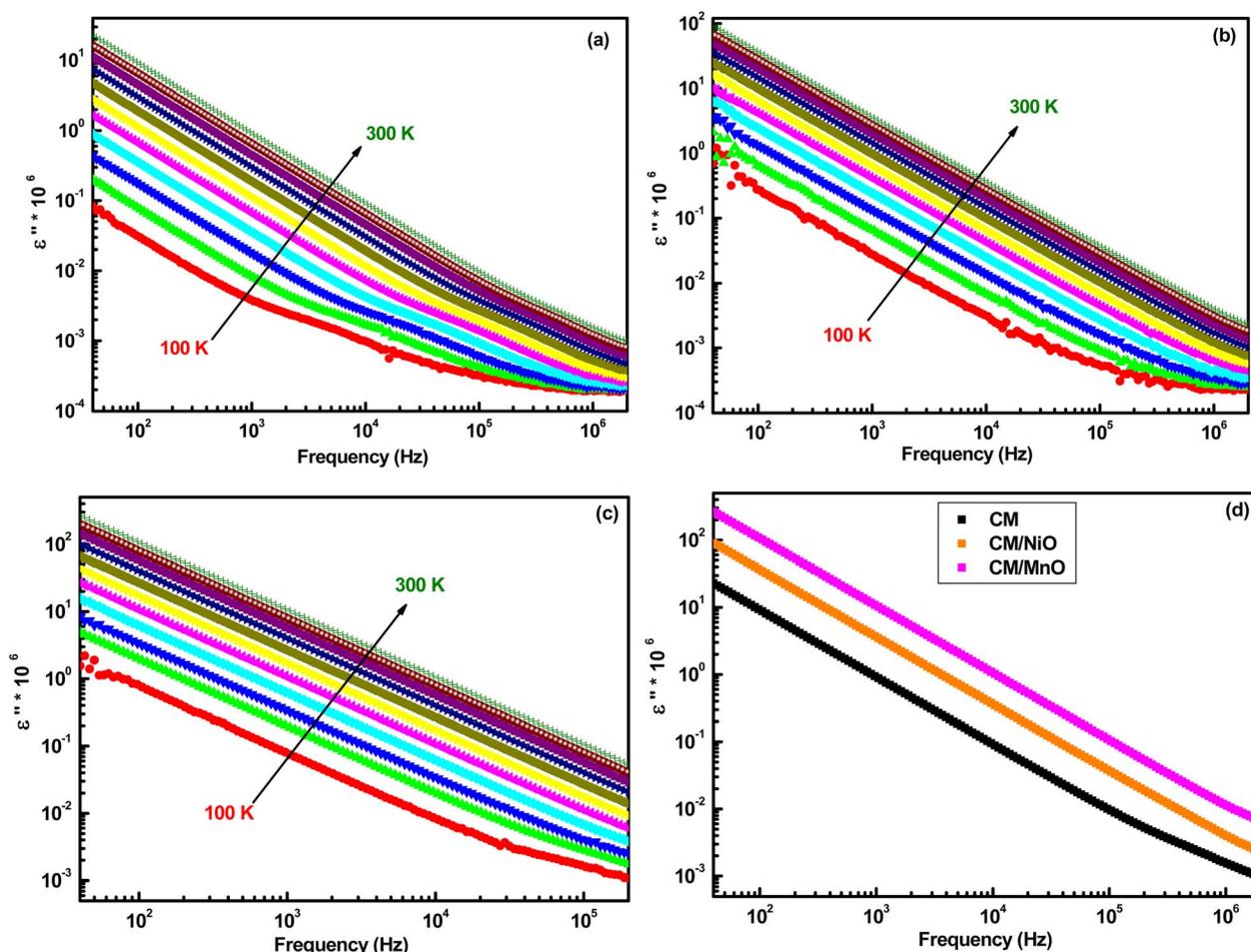

Fig. 18 Frequency dependence of the imaginary component of permittivity (ε'') for (a): CM, (b): CM/NiO, and (c): CM/MnO at various measurement temperatures with a step of 20 K and (d): at room temperature.
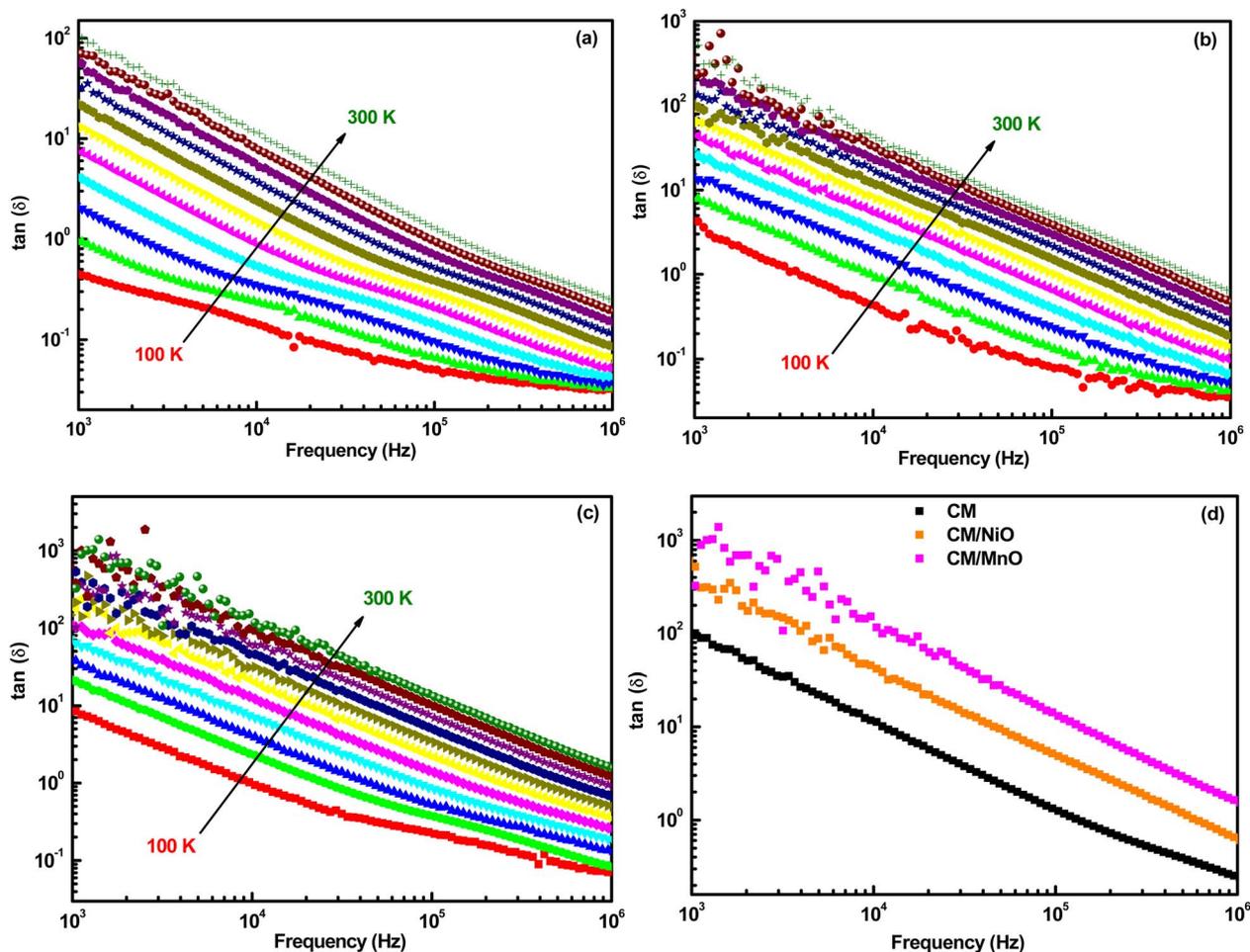
Fig. 19 Dependence of the dissipation factor (tan δ) with frequency at various measurement temperatures (20 K steps) for (a) CM, (b) CM/NiO, (c) CM/MnO and (d) at room temperature.

which rise significantly with increasing temperature as a result of thermally activated charge carriers and the conductive pathways provided by metallic Ni nanoparticles. The rapid decline in ε'' at higher frequencies reflects the progressive suppression of slow relaxation mechanisms. This behavior is in accordance with the trend observed for ε' and confirms the crucial role of the incorporated metal oxides, along with chlorine-related defect states, in governing both polarization and conduction processes.

Analyzing the imaginary component of permittivity (ε'') provides a deeper understanding of the energy loss mechanisms in the studied materials. To further investigate these dielectric losses and their dependence on frequency and temperature, it is useful to examine the dissipation factor (tan δ), which represents the ratio of the energy dissipated and the energy stored in the material. The dissipation factor is obtained from the relation:

$$\text{Tan } \delta = \frac{\varepsilon''}{\varepsilon'} \tag{7}$$

Tan δ of our materials is highly influenced by the type and distribution of the incorporated metal oxide (Fig. 19). Its

frequency and temperature dependence follow the Maxwell–Wagner model. At low frequencies and high temperatures, tan δ increases due to interfacial and thermally activated conduction, whereas the decrease at high frequencies reflects limited dipolar relaxation. In the CM/MnO nanocomposite, the significant rise in tan δ suggests that MnO promotes local conductive regions or trap states, enhancing charge mobility at grain interfaces. Conversely, CM/NiO shows reduced dielectric losses, likely resulting from metallic Ni nanoparticles that enhance structural stability and promote a more uniform microstructure. CM exhibits the lowest losses, reflecting its homogeneous structure.

These results highlight that the dielectric behavior of pyrogallol-formaldehyde-based nanocomposites is governed by interfacial polarization, conduction processes and microstructure. Thus, the controlled incorporation of metal oxide nanoparticles offers an effective strategy to tune the properties for energy storage and high-performance capacitor applications.

4. Conclusion

In this work, a pyrogallol-formaldehyde-derived carbon matrix (CM) and its nanocomposites incorporating NiO and MnO

nanoparticles were successfully synthesized *via* a sol–gel route, followed by pyrolysis. Structural analyses confirmed the amorphous nature of CM, formation of metallic Ni nanoparticles in the CM/NiO nanocomposite and thermal stability of MnO in the CM/MnO nanocomposite. XPS shows a preserved carbon structure, surface NiO and MnO species at the carbon interface, and residual chloride in the CM/MnO nanocomposite. Raman spectroscopy revealed that the incorporation of metal oxides increases structural disorder, with the CM/MnO nanocomposite exhibiting the highest defect density ($I_D/I_G = 1.53$), consistent with enhanced charge carrier localization. Electrical measurements demonstrated that both NiO and MnO significantly improve charge transport compared to the pristine CM. The CM/MnO nanocomposite showed the highest conductivity and lowest activation energy (80 meV), owing to Mn^{2+}/Mn^{3+} redox activity and a strongly defective carbon network. Impedance and dielectric analyses confirmed that the non-Debye relaxation was governed by Maxwell–Wagner interfacial polarization. Charge transport proceeds through correlated barrier hopping (CBH) in the CM/NiO nanocomposite, while thermally activated small polaron hopping (SPH) dominates in the CM/MnO nanocomposite. Although secondary, chlorine contributes to the defect landscape of the CM/MnO nanocomposite, creating additional sites that lower the hopping barrier for small polarons and enhance electrical conductivity and dielectric response. Therefore, by combining high conductivity, strong interfacial polarization and a low activation energy, the CM/MnO nanocomposite is a potential candidate for advanced electronic, dielectric and energy storage devices.

Author contributions

N. Ben Mansour performed the synthesis of the materials, contributed to the interpretation of the results, and wrote the manuscript. M. Hjiri and Rageh K. Hussein were involved in material characterization and data analysis. L. El Mir contributed to the interpretation of the results and manuscript revision.

Conflicts of interest

The authors declare that they have no conflict of interest.

Data availability

All data are available on request.

Acknowledgements

References

1 L. Yang, W. Li, S. Chen, Q. Luo, H. Wang, Z. Mao, Z. Liu, J. Yuan and G. He, *J. Cleaner Prod.*, 2025, **528**, 146732.

2 T. Khandaker, T. Islam, A. Nandi, M. A. A. M. Anik, M. S. Hossain, M. K. Hasan and M. S. Hossain, *Sustainable Energy Fuels*, 2025, **9**, 693.

3 Z. Mao, Y. Fu, X. Long, C. Li, M. Li, F. Zhu, W. Ye, Z. Fan and X. Yao, *Chem. Synth.*, 2025, **5**, 68.

4 N. Priyantha and M. Karunathilake, *Carbon: Bulk-To-Nano Forms for Detection and Remediation of Environmental Contaminants*, 2025, p. 1.

5 J. Chen, S. Wu, X. Hou, W. Song, Q. Guanxu, Z. Xu, K. Jin, Y. Yang and H. Zhang, *J. Mater. Chem. C*, 2025, **13**, 10454.

6 H. Fu, A. Mojiri, J. Wang and Z. Zhao, *Energies*, 2025, **18**(15), 3958.

7 P. Zhang, B. Zhu, P. Du and J. T. Sejdic, *Chem. Rev.*, 2024, **124**(3), 722.

8 S. A. Thomas, J. Cherusseri and D. N. Rajendran, *RSC Sustainability*, 2025, **3**, 219.

9 I. Raya, H. H. Kzar, Z. H. Mahmoud, A. A. A. Ahmed, A. Z. Ibatova and E. Kianfar, *Carbon Lett.*, 2022, **32**, 339.

10 I. Alali, A. U. Shehu and R. Mokaya, *Energy Environ. Sci.*, 2024, **17**, 5024.

11 L. Zhang, Y. Lei, P. He, H. Wu, L. Guo and G. Wei, *Nanomaterials*, 2022, **12**(18), 3172.

12 Li. Tao, Y. Wang, Y. Zou, N. Zhang, Y. Zhang, Y. Wu, Y. Wang, R. Chen and S. Wang, *Adv. Energy Mater.*, 2020, **10**, 1901227.

13 Z. Duan and G. Henkelman, *J. Phys. Chem. C*, 2020, **124**(22), 12016.

14 I. Østrøm, M. Favaro, M. Seyfouri, P. Burr and B. Hoex, *J. Am. Chem. Soc.*, 2025, **147**(4), 3593.

15 M. Bonomo, D. Dini and F. Decker, *Front. Chem.*, 2018, **6**, 601.

16 S. Park, Y. H. Lee, S. Choi, H. Seo, M. Y. Lee, M. Balamurugan and K. T. Nam, *Energy Environ. Sci.*, 2020, **13**, 2310.

17 P. Wang, S. Zhang, Z. Wang, Y. Mo, X. Luo, F. Yang, M. Lv, Z. Li and X. Liu, *J. Mater. Chem. A*, 2023, **11**, 5476.

18 K. O. Egbo, M. Kong, C. P. Liu and K. M. Yu, *J. Alloys Compd.*, 2020, **835**, 155269.

19 H. J. Seok, J. H. Park, A. Yi, H. Lee, J. Kang, H. J. Kim and H. K. Kim, *ACS Appl. Energy Mater.*, 2021, **4**(6), 5452.

20 R. Eppstein and M. C. Toroke, *ACS Mater. Au*, 2022, **2**(3), 269.

21 W. Li, Y. Xian, H. Deng, J. Xu, Y. Wei, A. Chang and B. Zhang, *J. Adv. Ceram.*, 2025, **14**(10), 9221153.

22 W. Djeridi, N. Ben Mansour, A. Ouederni, P. L. Llewellyn and L. El Mir, *Int. J. Hydrogen Energy*, 2017, **42**(13), 8905.

23 N. Ben Mansour, W. Djeridi and L. El Mir, *J. Inorg. Organomet. Polym. Mater.*, 2019, **29**(1), 192.

24 N. Ben Mansour, M. Hjiri, N. Mustapha, F. M. Barakat, T. F. Qahtan and L. El Mir, *RSC Adv.*, 2025, **15**, 32560.

25 H. Schmidt, G. Jonschker, S. Goedicke and M. Mennig, *J. Sol-Gel Sci. Technol.*, 2000, **19**, 39.

26 X. Guo, Q. Zhang, X. Ding, Q. Shen, C. Wu and L. Zhang, Hui Yang, *J. Sol-Gel Sci. Technol.*, 2016, **79**, 328.

27 H. Ikake, S. Hara and S. Shimizu, *Polymers*, 2022, **14**(16), 3247.

28 M. Sivakumar, V. Veeramani, S. M. Chen, R. Madhu and S. B. Liu, *Microchim. Acta*, 2019, **186**(59), 186.

29 A. S. Justin, P. Vickraman and B. J. Reddy, *J. Electroanal. Chem.*, 2018, **823**, 342.

30 A. R. Seitkazinova, M. Nazhipkyzy, K. Kudaibergenov, A. Issanbekova, N. S. Bergeneva, A. Abdisattar and M. Kyzgarina, *J. Compos. Sci.*, 2025, **9**(10), 561.

31 J. Singh, A. Choudhury, Md.W. Ahmad, A. Syed, S. Khan, H. A. ALShwaiman, L. S. Wong and D. J. Yang, *Surfaces and Interfaces*, 2025, **56**, 105736.

32 S. Guo, G. Lu, S. Qiu, J. Liu, X. Wang, C. He, H. Wei, X. Yan and Z. Guo, *Nano Energy*, 2014, **9**, 41.

33 G. Nagaraju, P. Santhoshkumar, S. C. Sekhar, B. Ramulu, M. Nanthagopal, P. S. S. Babu, C. W. Lee and J. S. Yu, *J. Power Sources*, 2022, **549**, 232113.

34 M. Wayu, *Solids*, 2021, **2**(2), 232.

35 L. El Mir, S. Kraiem, M. Bengagi, E. Elaloui, A. Ouderni and S. Alaya, *Phys. B: Condens. Matter*, 2007, **395**, 104.

36 L. El Mir, N. Ben Mansour, I. Najeh, M. Saadoun and S. Alaya, *Int. J. Nano Biomater.*, 2009, **2**, 249.

37 F. Sayari, N. Ben Mansour, M. Kraini, M. A. Wederni, M. Hjiri, F. Aouaini, A. Sharma and L. El Mir, *J. Inorg. Organomet. Polym. Mater.*, 2025, **35**, 98.

38 A. M. Aldawsari, M. N. Shaddad and S. A. Aladeemy, *Catalysts*, 2025, **15**(7), 662.

39 D. D. Yadav, A. Kumar, R. Jha and S. Singh, *ECS J. Solid State Sci. Technol.*, 2025, **14**, 077005.

40 J. Peng, L. Giordano, T. C. Davenport and Y. S. Horn, *Chem. Mater.*, 2022, **34**(17), 7774.

41 T. D. Schladt, T. Graf and W. Tremel, *Chem. Mater.*, 2009, **21**, 3183.

42 J. Dai, D. Wei, Z. Wang, L. Si, S. Cao, H. Liu and Z. Ye, *Ceram. Int.*, 2025, **51**(4), 5434.

43 C. Jung, H. Jun, K. Jang, S. H. Kim and P. P. Choi, *Microsc. Microanal.*, 2022, **28**(6), 1841.

44 N. Ben Mansour and L. El Mir, *J. Phys. Chem. Solids*, 2019, **127**, 1.

45 W. Ahmed, H. Jeidi, W. Djeridi, N. Ben Mansour, P. L. Llewellyn, H. Dahman and L. El Mir, *Indian J. Phys.*, 2023, **97**, 1769.

46 N. Ben Mansour, M. Hjiri, W. Djeridi and L. El Mir, *RSC Adv.*, 2025, **15**, 12076.

47 N. Ben Mansour and L. El Mir, *Appl. Surf. Sci.*, 2014, **308**, 10.

48 N. Ben Mansour, W. Djeridi and L. El Mir, *J. Inorg. Organomet. Polym. Mater.*, 2021, **31**, 4360.

49 N. F. Mott and E. A. Davis, *Electronic Processes in Non Crystalline Materials*, Clarendon, Oxford, 1979, p. 157.

50 A. K. Jonscher, *Nature*, 1977, **276**, 673.

51 A. Radon, D. Lukowiec, M. Kremzer, J. Mikula and P. Wlodarczyk, *Materials*, 2018, **11**(5), 735.

52 Y. Ben Taher, A. Oueslati, N. K. Maaloul, K. Khirouni and M. Gargouri, *Appl. Phys. A*, 2015, **120**, 1537.

53 M. Javed, A. A. Khan, J. Kazmi, M. A. Mohamed, M. N. Khan, M. Hussain and R. Bilkees, *Mater. Res. Bull.*, 2021, **138**, 111242.

54 S. M. Gateman, O. Gharbi, H. G. de Melo, K. Ngo, M. Turmine and V. Vivier, *Curr. Opin. Electrochem.*, 2022, **36**, 101133.

55 S. Sahoo, A. S. Priya, S. Anwar and S. Anwar, *Mater. Res. Bull.*, 2026, **198**, 114017.

56 I. Garoui, S. Ben Yahya, N. A. Alghamdi, I. Chaabane, A. Oueslati and B. Louati, *Mater. Adv.*, 2025, **6**, 9761.

57 S. Smii, Y. Moualhi, F. Bahri and H. Rahmouni, *Phys. B*, 2023, **662**, 414966.